ParCFD'2019
31^{st} International Conference on Parallel Computational Fluid Dynamics
May-14-17 2019, Antalya TURKEY

EXPERIENCES WITH PARALLEL ICE ACCRETION SIMULATIONS OF AIRPLANE WINGS USING OPENFOAM – PARCFD'2019

SEGHAER H. EDEEB*, HASAN U. AKAY AND SERKAN OZGEN †**

* Atilim University
Department of Modeling and Design of Engineering Systems (MODES)
06830 Ankara, TURKEY
e-mail: edeeb.seghaer@student.atilim.edu.tr - Web page: http://www.atilim.edu.tr/en

**Atilim University
Department of Mechanical Engineering
06830 Ankara, TURKEY
e-mail: hasan.akay@atilim.edu.tr - Web page: http://www.atilim.edu.tr

† Middle East Technical University (METU)
Department of Aerospace Engineering
06800 Ankara, TURKEY
e-mail: serkan.ozgen@ae.metu.edu,.tr, Web page: http://www.metu.edu.tr

Key words: OpenFOAM, parallel computation, supercooled droplets, ice accretion, aerodynamic coefficients.

Abstract. Ice accretion on aircraft components starts when an aircraft flies through atmospheric clouds containing supercooled liquid droplets, which have a temperature below freezing point but are still in a liquid state. Ice accretion occurs when water droplets impinge and freeze on the unprotected frontal regions of aircraft surfaces. The accumulated ice on aircraft components degrades the aircraft performance and causes serious flight problems. In this study, a computational fluid dynamics package is developed using open-source software. The created package is used to predict rime and glaze ice shapes on a wing airfoil for different icing condition cases. The results show a satisfactory agreement in ice shape prediction obtained using the OpenFOAM and the developed code THERMSOLVICE with the corresponding data in the literature. The effects of the formed ice on the aerodynamic performance are also investigated, showing significant changes at high angles of attack.

1 INTRODUCTION

Ice accretion takes place on aircraft components such as the wing, tail, and engine inlet during flight through clouds containing supercooled water droplets. Although the ambient temperature is below the freezing temperature in the range between $-40\ ^oC$ and $0\ ^oC$, supercooled droplets tend to remain in a liquid phase due to the absence of solid particles in the atmosphere. Dust, smoke particles and salt crystals suspended in the air function as nuclei needed for the solidification process. Based on many icing factors

such as ambient temperature, liquid water content and supercooled droplet diameter, ice accretion begins to occur as soon as supercooled droplets impinge the unprotected areas of the aircraft surfaces [1]. As a result, the aerodynamic shape of the airfoil changes, causing a reduction in the lift coefficient and an increase in the drag coefficient, thereby reducing aircraft performance [2]. The accumulated ice on the aircraft surfaces can be generally classified into two types: rime ice and glaze ice. The former is typically formed at low-ambient temperatures, low liquid water content (LWC) and low droplet median volume diameter (MVD), when supercooled droplets impinge on the wing's leading edge and freeze immediately and entirely. Rime ice is characterized by low density, opaque, soft, milky appearance and exhibits streamlined shapes [3]. Glaze ice is formed at ambient temperatures just below freezing, high air liquid water content, high relative impact speed and large water droplet diameters. Supercooled droplets in glaze ice conditions do not freeze completely in the impingement zone, and a portion of the water droplets remains in a liquid phase and runs back along the airfoil surface. Glaze ice is characterized by higher density, transparent and irregular shape with protrusions [4].

Although there are a few institutional and commercial ice accretion simulation packages available in numerical ice prediction community, such as LEWICE by NASA (National Aeronautics and Space Administration), DRA by Defense Research Agency in England, ONERA by the Office National D'etudes Et de Recherches Aerospatiales in France, CANICE by Bombardier Aerospace in Canada, TAICE by Turkish Aerospace Industry in Turkey and FENSAP by ANSYS in USA, there is no major ice accretion simulation package available in the open-source software area. As such, our goal in the present work is to develop an integrated ice accretion simulation package using the available modules of OpenFOAM, and to make improvements on those modules for fast and accurate simulations. For pre-processing and post-processing of solutions and ice accretion calculations, only open-source software is used with the assertion that this approach has the potential for improving the prediction of ice formation on aircraft components, making room for other studies to contribute to the field. Parallel processing techniques are used to accelerate the computation rate and to distribute the computing time through all parallel computers. In OpenFOAM, the method of computation with parallel computers is known as domain decomposition. The domain geometry and the related fields are broken into sub-domains and allocated to processors for solving. Parallelization process in OpenFOAM consists of: decomposition of the case domain, running the case in parallel, and post-processing of the case solution. Message Passing Interface software (MPI) is used for parallel running and communicating between computers.

2 Methodology

2.1 Stages of the Method

Ice accretion on aircraft surfaces is an unsteady and moving boundary phenomenon, even in steady flow conditions. Starting with the initial conditions, the equations have to be numerically integrated in time with Δt time increments until the end of accretion process. The major stages of calculations for ice accretion on aerodynamic bodies consist

of: 1) preparation of geometry, 2) generation of computational mesh, 3) setting up initial conditions, 4) solution of flow equations, 5) calculation of droplet trajectories and collection efficiencies, 6) thermodynamic analysis for ice thickness calculations, 7) modification of geometry due to ice thickness formation, 8) regeneration of the mesh for modified geometry, and 9) advancing in time and repeating steps 4 thru' 9 until the end of the exposure time. Typically, the geometry of the body changes after each time step as water droplets freeze on the body surface. Hence, theoretically mesh updates close to the body are needed after each time step. However, since this is computationally expensive and that geometry changes are relatively small, the mesh updates are made after several time steps forming multiple layers, or even never, during the exposure time of the simulations depending on the flow and icing conditions, as will be demonstrated with examples.

2.2 Open-Source Software Used

In the development of the icing simulation package for the present study, the authors decided to stay strictly with open-source software, the most prominent one of which is OpenFOAM which is a finite volume-based software designed to simulate a variety of continuum mechanics problems [5]. It includes specialized solvers for incompressible flow, compressible flow, conduction heat transfer, conjugate heat transfer, electrodynamics, solid dynamics, etc. For fluid flows, various solvers are available such as potentialFoam for potential flow, simpleFoam for viscous incompressible flow and sonicFoam for viscous compressible flow [6]. For flow simulations of ice accretion, we use the incompressible flow code simpleFoam since ice accretion occurs mainly in incompressible regimes. A Lagrangian solver named 'icoUncoupledKinematicParcelFoam' is used to compute droplet trajectories. To predict ice and water layer formations, a model called 'Extended Messinger Model' for heat and mass transfer [7] is applied to flow and trajectory calculations, where Octave library is used as a high-level open-source programming language for scientific computing. Octave library has a large number of built-in functions for numerical solutions and graphical visualizations similar to MATALAB package[8]. Using Octave library, THERMSOLVICE code is developed to calculate the thickness of ice and water layers formed on the airfoil surface and the temperature distribution taking place across these layers. The other open-source packages used in this study include GMSH, which is a geometry and mesh generation software and PARAVIEW, which is a visualization software.

3 Fluid Flow Solution

3.1 Geometry Creation and Mesh Generation

In this study, NACA 0012 airfoil is selected because of the availability of detailed numerical and experimental icing data related to the subject in the literature. GMSH is used to draw the airfoil geometry and generate the computational meshes. The computational domain dimensions are extended far away from the airfoil to eliminate any effect related to farfield boundaries in the solution. The mesh points are clustered and made fine around the airfoil surface in order to obtain an accurate fluid flow solution close to the airfoil wall as shown in Figure 1, where the chord length is 0.53 m in the test cases

solved. The mesh used has about 1.5 million tetrahedral finite volume cells. Due to the two-dimensional nature of the problem on the x-y plane, only one layer of tetrahedrals is used in the z-direction with appropriate boundary conditions applied on the z-surfaces.

3.2 Fluid Flow Simulation

The simpleFoam solver used here is a steady state, incompressible, laminar and turbulent flow solver. The selected icing condition cases are considered as two-dimensional, thus requiring no computation in the z-direction. The mesh file created using GMSH with its boundary conditions is converted to foam format by an OpenFOAM command. The solution of the incompressible flow around the airfoil starts with defining three folders in incompressible solver in OpenFOAM. The folders used as the input data are defined with 0, constant and system. In the 0 folder, the initial values of pressure and velocity are defined at all boundary conditions for the simulated case. The boundaries of the computational domain are defined as inlet, outlet, topandbottom, frontandback, and airfoilwall. All physical properties must be defined at these boundaries. The variable parameters for these cases are defined at the inlet/outlet boundaries by free stream velocity, at airfoil wall by no-slip condition, and by empty for the faces in the z-direction. The constant folder contains a polyMesh folder, where the meshing process is completely defined. The transport and turbulence properties are also defined in the constant folder. The system folder has three control files: fvSchemes, fvSolution, and controlDict files. The fvSchemes file is for selecting discretization schemes, the fvSolution file is for relaxation and conversion parameters, and the controlDict file for controlling the simulation time and output data. The Spalart Allmaras model is used to simulate the flow turbulence properties. Gauss linear and Gauss linear upwind are used for Navier-Stokes equations discretization. SIMPLE (Semi-Implicit Method for Pressure-Linked Equations), GAMG (Generalized Geometric-Algebraic Multi-Grid), and Gauss Seidel methods are used for solving the governing equations and smoothing the solution. The following form of incompressible flow equations are solved: [9]:

Continuity equation

$$\nabla \cdot \overrightarrow{V} = 0 \tag{1}$$

Momentum equation

$$\rho \frac{D\overrightarrow{V}}{Dt} = \rho g - \nabla p + \mu \nabla^2 \overrightarrow{V} \tag{2}$$

where ρ is the density (kg/m^3), p is the pressure (N/m^2), $\overrightarrow{V}$ is the velocity vector (m/s), μ is dynamic viscosity ($kg/m \cdot s$), g is gravitational acceleration (m/s^2) and t is time (s).

3.3 Calculation of Convective Heat Transfer Coefficients

The OpenFOAM utility wallGradU is a post-processing command used to compute the velocity gradient for each mesh point along the airfoil surface. PARAVIEW is used as a post-processing tool coupled with OpenFOAM and also to extract the values of velocity

gradient and kinematic viscosity at all airfoil surface meshes to compute the wall shear stress at the airfoil surface from:

$$\tau = \mu \left.\frac{du}{dy}\right|_{y=0} = \nu\rho \left.\frac{du}{dy}\right|_{y=0} \tag{3}$$

where τ is the wall shear stress, μ is the air dynamic viscosity, $\left.\frac{du}{dy}\right|_{y=0}$ is the velocity gradient in the normal direction of the airfoil surface, ρ is the air density and ν is the air kinematic viscosity. The convective heat transfer coefficient is an important parameter to accurately predict the shape and thickness of the ice and water layers. The heat transfer coefficient is calculated from wall shear stress using the Reynolds analogy formula [10]. The main parameters through the boundary layers as shown in Figure 2 are the shear stress and molecular conduction heat transfer. According to Reynolds analogy, the heat transfer coefficient can be obtained from the analogy of heat flux and momentum transfer. The convective heat transfer coefficient for the laminar or turbulent boundary layer can be computed using the equation below:

$$h_c \approx \rho_\infty u_\infty C_p C_f/2 \tag{4}$$

where h_c is the convective heat transfer coefficient, ρ_∞ is the free stream density, u_∞ is the free stream velocity, C_p is the air specific heat and C_f is the skin friction coefficient computed from wall shear stress.

4 Calculation of Water Droplet Trajectories

4.1 Possible Approaches

Trajectory computation of supercooled water droplets is the second module of ice accretion prediction package. Droplet trajectories can be simulated using either a Lagrangian or an Eulerian approach. In the Lagrangian approach, the trajectory of each droplet must be tracked from the initial releasing until it either hits the airfoil surface or escapes from it. The trajectory is calculated by solving the governing equations of droplet's motion based on Newton's second law. The acting forces on the water droplets are gravity, buoyancy, and drag forces. The air velocity distribution obtained from the fluid flow solution around the airfoil is required to solve the droplet trajectory. In the Eulerian method, two phases are used where the water droplets are considered as a separate phase within the air phase. Water droplet continuity and momentum equations are solved with the governing equations of air flow to determine the droplet and impacting regions. In this work, the Lagrangian approach is selected [11, 12, 13, 14].

4.2 Lagrangian Approach

In this approach, water droplets are considered spherical in shape and they do not affect the air flow. The governing equations are [15]:

$$m\frac{d^2x_p}{dt^2} = -D\ cos\gamma + mg\ sin\gamma \tag{5}$$

$$m\frac{d^2y_p}{dt^2} = -D\ sin\gamma + mg\ cos\gamma \tag{6}$$

$$\gamma = tan^{-1}\left(\frac{\dot{y}_p - v}{\dot{x}_p - u}\right) \tag{7}$$

where x_p and y_p are the droplet position coordinates, $\dot{x}_p$ and $\dot{y}_p$ are the droplet velocity components, u and v are the air flow velocity components, γ is the angle between the droplet velocity and air flow velocity, and α is the angle of attack. The drag force (D) is a function of drag coefficient (C_D), droplet cross section area A_p, air density ρ and the relative velocity V of droplets.

$$D = \frac{1}{2}\rho V^2 A_p C_D \tag{8}$$

Relative velocity (V) is a function of air and droplet velocities:

$$V = \sqrt{(\dot{x}_p - u)^2 + (\dot{y}_p - v)^2} \tag{9}$$

Drag coefficient (C_D) is based on Reynolds number (Re) [16]:

$$C_D = \frac{24}{Re}(1 + 0.197Re^{0.63} + 2.6\times10^{-4}\times Re^{1.38}) \quad for\ \ Re \leq 3500 \tag{10}$$

$$C_D = \frac{24}{Re}(1.699\times10^{-5} \times Re^{1.92}) \quad for\ \ Re > 3500 \tag{11}$$

For droplet trajectory calculations, OpenFOAM Lagrangian solver icoUncoupledKinematicParcelFoam is selected as a transient solver for the passive transport of a single kinematic particle cloud requiring a flowfield solution as the required data. For multi-layer calculations, this solver can be used after flowfield calculations for each layer. It is one-way coupling, where there is no effect from water droplets on the air flow. It has a high capacity to couple with the flowfield variables. Many parameters of this solver can be modified such as: particles cloud properties, positions, and collision. [15, 6].

4.3 Collection Efficiency Calculation

In the Lagrangian approach, the water droplets are arranged in a vertical line far upstream the airfoil leading edge, and their motion starts when they are released and tracked until impacting the airfoil surface or escaping away. The obtained output data from the trajectory calculations are the number of impacting droplets, their mass and locations on the airfoil surface. By using the PARAVIEW program, the coordinates of the impacting droplets are extracted and used to determine an important icing parameter refered to as the 'collection efficiency (β)'. In the simulation, water droplet particles released far away from the airfoil leading edge initially have a fixed distance between them ($\triangle Y = 0.0009434C$, where C is the airfoil chord length) and they move in downstream direction under the effect of air velocity. In the cases analyzed here, the vertical line

is placed about 9.434 chord lengths upstream from the leading edge of the airfoil and chord lengths above and below the mid-surface of the airfoil. Typically, 8,000 droplets are released from the initial position, forming a vertical line of clouds of length $7.547C$. For a positive angle of attack, the intensity of impinging droplets is high at the lower surface behind the leading edge and decreases along the upper and lower airfoil surfaces downstream. The collection efficiency values β along the impacting surface are calculated using the following equation:

$$\beta = \frac{\triangle Y}{\triangle S} \tag{12}$$

where $\triangle Y$ is the vertical distance between two droplets at the releasing or injection position, and $\triangle S$ is the corresponding distance between the same droplets along the airfoil impingement surface.

5 Thermodynamic Model

5.1 Extended Messinger Model

In order to predict ice and water layer thicknesses which are indicated schematically in Figure 3, mass and heat balances are required for each control volume along the upper and lower airfoil surfaces. The icing process on the airfoil surface is based on the phase-change phenomenon (Stefan problem). The Extended Messinger Model is used to simulate the governing equations of mass and heat fluxes [7].

The governing equations of the icing process [17] are:

The energy equation in the ice layer:

$$\frac{\partial T}{\partial t} = \frac{k_i}{\rho_i C_{pi}} \frac{\partial^2 T}{\partial y^2} \tag{13}$$

The energy equation in the water layer:

$$\frac{\partial \theta}{\partial t} = \frac{k_w}{\rho_w \ C_{pw}} \frac{\partial^2 \theta}{\partial y^2} \tag{14}$$

The conservation of mass equation:

$$\rho_i \ \frac{\partial B}{\partial t} + \rho_w \ \frac{\partial h}{\partial t} = \rho_a \beta v_\infty + \dot{m}_{in} - \dot{m}_{e,sub} \tag{15}$$

The phase change equation at the ice/water interface:

$$\rho_i \ L_F \ \frac{\partial B}{\partial t} = k_i \ \frac{\partial T}{\partial y} - k_w \ \frac{\partial \theta}{\partial y} \tag{16}$$

where T and θ are the temperatures, k_i and k_w are the thermal conductivities, and C_{pi} and C_{pw} are the specific heats of ice and water layers, respectively. B is the ice layer thickness and h is the water layer thickness, $\rho_a \beta v_\infty$ is the impinging mass of the water

droplets, $\dot{m}_{in}$ is the mass entering control volumes due to the runback water, $\dot{m}_{e,sub}$ is either the mass of the evaporated or sublimated water depending on the conditions, ρ_i and L_F are the ice density and latent heat generated due to solidification. The ice density has two values: ρ_r is the rime ice density and ρ_g is the glaze ice density.

5.2 Initial and Boundary Conditions

The following assumptions are used to calculate ice and water thicknesses and temperature distributions through them:

- The ice is in perfect contact with the airfoil surface and is taken to be equal to the ambient temperature T_a.

$$T(0,t) = T_s = T_a \tag{17}$$

- The temperature is continuous at the ice/water interface boundary and it is equal to the freezing temperature T_f.

$$T(B,t) = \theta(B,t) = T_f \tag{18}$$

- At the ice/air interface (rime ice) and water/air interface (glaze ice) boundaries, the heat transfer flux per unit area is determined by:

$$-k_i \frac{\partial T}{\partial y} = (Q_c + Q_d + Q_s + Q_r) - (Q_a + Q_k + Q_{in} + Q_l) \qquad at \quad y = B \tag{19}$$

$$-k_w \frac{\partial \theta}{\partial y} = (Q_c + Q_d + Q_e + Q_r) - (Q_a + Q_k + Q_{in}) \qquad at \quad y = B + h \tag{20}$$

  where $Q_c, Q_d, Q_s, Q_e, Q_r, Q_a, Q_k, Q_l$ and Q_{in} are the energy fluxes defined in Section 5.3.

- The airfoil is initially clean at time $t = 0$, ice thickness $(B) = 0$ and water layer height $(h) = 0$.

5.3 Calculation of Heat Fluxes

The heat transfer fluxes associated with the phenomenon [7, 17] are expressed using the following formula:

Heat loss by convection (Q_c)

$$Q_c = h_c(T_{sur} - T_a) \tag{21}$$

where h_c is the convective heat transfer coefficient, T_{sur} is the surface temperature, and T_a is the ambient temperature.

Cooling by incoming droplets (Q_d)

$$Q_d = \rho_a \beta v_\infty C_{pw}(T_{sur} - T_a) \tag{22}$$

Heat loss by evaporation (Q_e)

$$Q_e = X_e \epsilon_0 (T_{sur} - T_a) \quad and \quad X_e = \frac{0.622 h_c L_E}{C_p P_t L_e^{2/3}} \tag{23}$$

where $\epsilon_0 = 27.03$ is the saturation vapor pressure constant, P_t is the free stream total pressure, L_E is the latent heat of evaporation and L_e is the Lewis number.

Heat loss by sublimation (Q_s)

$$Q_s = X_s \epsilon_0 (T_{sur} - T_a) \quad and \quad X_s = \frac{0.622 h_c L_s}{C_p P_t L_e^{2/3}} \tag{24}$$

where $\epsilon_0 = 27.03$, P_t is the free stream total pressure, L_s is the latent heat of sublimation and L_e is the Lewis number.

Heat loss by radiation (Q_r)

$$Q_r = 4\epsilon \sigma_r {T_a}^3 (T_{sur} - T_a) \tag{25}$$

where ϵ is the surface emissivity and σ_r is the Stefan-Boltzmann constant.

Heat gain by aerodynamic heating (Q_a)

$$Q_a = \frac{r h_c {v_\infty}^2}{2 C_{pa}} \tag{26}$$

Heat gain by the kinetic energy of incoming droplets (Q_k)

$$Q_k = \frac{1}{2} \rho_a \beta {v_\infty}^3 \tag{27}$$

Heat brought by runback water (Q_{in})

$$Q_{in} = \dot{m}_{in} C_{pw}(T_{sur} - T_a) \tag{28}$$

Latent heat of solidification (Q_l)

$$Q_l = \rho_r L_F \frac{\partial B}{\partial t} = L_F(\rho_a \beta v_\infty + \dot{m}_{in} - \dot{m}_{sub}) \tag{29}$$

where T_{sur} is the temperature at ice surface for the rime ice or at water surface for the glaze ice.

5.4 Rime Ice Thickness and Temperature Distribution in the Ice Layer

Using the conservation of mass equation 15, the rime ice thickness can be determined directly from the governing equation because all the impinging water freezes immediately. Under these conditions, the rime ice growth rate ($\frac{\partial B}{\partial t}$) is determined from equation 15 ($h = 0$):

$$\frac{\partial B}{\partial t} = \frac{\rho_a \beta v_\infty + \dot{m}_{in} - \dot{m}_{sub}}{\rho_r} \tag{30}$$

From which the rime ice thickness (B) is obtained as:

$$B(t) = \frac{\rho_a \beta v_\infty + \dot{m}_{in} - \dot{m}_{sub}}{\rho_r} \ t \tag{31}$$

For ice thickness less than 2.4 cm, which is the case for most applications [7], the temperature distribution is governed by

$$\frac{\partial^2 T}{\partial y^2} = 0 \tag{32}$$

Integrating equation 32 twice and using the boundary conditions, we obtain

$$T(y) = T_{sur} + \frac{(Q_a + Q_k + Q_{in} + Q_l) - (Q_c + Q_s + Q_d + Q_r)}{k_i + B(Q_c + Q_s + Q_d + Q_r)/(T_{sur} - T_a)} \ y \tag{33}$$

5.5 Glaze Ice Thickness and Temperature Distribution in Ice and Water Layers

The temperature distribution in the ice and water layers is governed by

$$\frac{\partial^2 T}{\partial y^2} = 0, \qquad \frac{\partial^2 \theta}{\partial y^2} = 0 \tag{34}$$

Integrating equation 34 twice and using the boundary conditions in equations 19 and 20 gives the temperature distribution in ice $T(y)$ and water $\theta(y)$ layers as follows:

$$T(y) = T_{sur} + \frac{(T_f - T_s)}{B} \ y \tag{35}$$

$$\theta(y) = T_f + \frac{(Q_a + Q_k + Q_{in}) - (Q_c + Q_e + Q_d + Q_r)}{k_w + h(Q_c + Q_e + Q_d + Q_r)/(T_f - T_a)} \ (y - B) \tag{36}$$

The water layer height expression $h(t)$ can be obtained by integrating once the equation of mass conservation as follows:

$$h(t) = \frac{\rho_a \beta v_\infty + \dot{m}_{in} - \dot{m}_e}{\rho_w} \ (t - t_g) - \frac{\rho_g}{\rho_w} \ (B - B_g) \tag{37}$$

where B_g is the ice thickness at the first appearance of glaze ice and t_g is the corresponding time.

If equations 35 and 36 are inserted into equation 16, the following first order differential equation is obtained for calculating glaze ice thickness.

$$\rho_g \ L_F \ \frac{\partial B}{\partial t} = \frac{K_i \ (T_f - T_s)}{B} - k_w \ \frac{(Q_a + Q_k) - (Q_c + Q_d + Q_e + Q_r - Q_{in})}{k_w + h \ (Q_c + Q_d + Q_e + Q_r - Q_{in}) \ / \ (T_f - T_a)} \quad (38)$$

The glaze ice thickness is found by solving the differential equation numerically using the Fourth-Order Runge-Kutta method in THERMSOLVICE code.

5.6 Freezing Fraction and Runback Water Strategy

In order to find the ice thickness at the first appearance of glaze ice B_g and the corresponding time t_g, the ice growth rate for both types is the same. At $B = B_g$, we have:

$$\left.\frac{\partial B}{\partial t}\right|_{rime} = \left.\frac{\partial B}{\partial t}\right|_{glaze} \quad (39)$$

Inserting equation 30 into equation 38 gives

$$B_g = \frac{k_i(T_f - T_s)}{(\rho_a \beta V_\infty + \dot{m}_{in} - \dot{m}_{sub})L_F + (Q_a + Q_k + Q_{in}) - (Q_c + Q_e + Q_d + Q_r)} \quad (40)$$

$$t_g = \frac{\rho_r}{(\rho_a \beta V_\infty + \dot{m}_{in} - \dot{m}_{sub})} B_g \quad (41)$$

Rime ice freezing fraction

$$FF = \frac{\rho_r B}{(\rho_a \beta V_\infty + \dot{m}_{in})t} = 1 \qquad for \quad t < t_g \quad (42)$$

Glaze ice freezing fraction

$$FF = \frac{\rho_r B + \rho_g (B - B_g)}{(\rho_a \beta V_\infty + \dot{m}_{in})t} < 1 \qquad for \quad t \geqslant t_g \quad (43)$$

Runback water initiates from all the unfrozen water running back along the upper airfoil surface to the neighboring downstream control volumes. For the lower surface, all runback water sheds under the effect of gravity.

Runback water mass flow rate ($\dot{m}_{out}$)

$$\dot{m}_{out} = (1 - FF)(\rho_a \beta V_\infty + \dot{m}_{in}) - \dot{m}_e \quad (44)$$

The evaporating mass ($\dot{m}_e$) and sublimating mass ($\dot{m}_{sub}$) equations are:

$$\dot{m}_e = \frac{Q_e}{L_E} \quad and \quad \dot{m}_{sub} = \frac{Q_s}{L_s} \quad (45)$$

6 Parallel Computation

Simulation with high performance of large size cases remains one of typical problems in the last decades. Parallel processing techniques are used to accelerate the computing rate and to share the processing memory with all parallel computers [25]. Parallel computation facility utilized in this work is Atilim University Computational Science and Engineering Laboratory ($CSE - LAB$). The specifications of this facility are: HP Proliant SL270s Gen8 MODEL, Single Node, 62 GB RAM and CPU of Intel® Xeon(R) CPU E5−680 v2 @ 2.8 GHZ ×20 and Graphical Card of Gallium 0.4 on llvmpipe (LLVM 4.0, 256 bits) + 2× NVIDIA TESLA K80 GPU. In OpenFoam, the method of computation with parallel computers is known as domain decomposition. The domain geometry and the related fields are broken into sub-domains and allocated to processors for solving. Parallelization process in OpenFoam consists of: decomposition of the case domain, running the case in parallel, and post-processing of the case solution. Message Passing Interface software (MPI) is used for parallel running and communicating between computers. The process of parallelization is started in OpenFOAM by decomposing the computational domain to a number of sub-domains equal to the available number of processors [26]. There are four methods of decomposing in OpenFoam: simple, hierarchical, scotch and manual. In simple and hierarchical methods, the domain split to sub-domains by specifying the number of pieces in each direction. Both are used for simple geometries. In scotch method, the computational domain is decomposed by specifying the weighting of the domain decomposition between the processors. It is used for complex geometries to minimize the number of faces between processors.

6.1 Sample Case of Parallel Processing

A simulation case of incompressible flow around airfoil for 100 iterations with 1,440,435 grids is taken as an example to illustrate the relation between the number of processors and the processing time. Table 1 shows the computation time and the corresponding number of processors used.

Comparing the results indicates that the increasing of the number of processors reduce the computational time. The reducing rate of the computational time is high with initial increase of the number of processors and becomes low or remains constant at high number of processors. The reasons of that are returned to the increase of communication time between the processors which affect the total computation time. Figure 4 shows the visualization of the computational domain using PARAVIEW program after decomposition to twenty sub-domains with scotch method.

6.2 Performance of Parallel Computing

Performance measuring method of parallel computing can be achieved by many parameters such as speedup parameter and parallel processing efficiency parameter. Speedup

Table 1: Parallel processing strategy

Number of processors	Computation time for 100 iterations (seconds)
1	1546.75
2	715.35
4	342.337
6	244.022
8	203.13
10	174.911
12	128.329
14	111.86
16	108.456
18	89.826
20	133.841

parameter (S_p) is defined as the ratio of the computation time of one processor (t_1) to the computation time when multi processors are used (t_p) [27]. Parallel efficiency parameter (E_p) is defined as the ratio of computing time of one processor to the time by multiple processors. The main advantage of using parallel computing is the reduction of the computing time.

$$S_p = \frac{Computing\ time\ using\ one\ processor}{Computing\ time\ using\ p\ processors} = \frac{t_1}{t_p} \tag{46}$$

$$E_p = \frac{Computing\ time\ using\ one\ processor}{Computing\ time\ by\ multiple\ processors} = \frac{S_p \times 100}{p} \tag{47}$$

Figure 5 shows the ideal and actual values of speedup parameter. Ideal curve represents the values of speedup parameter when the computation time is equally divided on the number of processors. Actual curve is obtained from the parallel processing computation results in Table 1. The speedup values increases linearly with increasing number of processors and with the same rate of ideal speedup values until fourteen processors. With increasing number of processors more than fourteen processors, the actual speedup values are increased non-linearly with increasing number of processors due to their communication time and the different number of grids in processors.

Performance efficiency curves illustrated in the Figure 6 show that the parallel processing technique improves the efficiency of computing for number of processors equal six processors or less. Reduction in performance efficiency is observed for number of processors more than six. There are some reasons for that such as increasing the time of communication between processors and unbalance of grids distribution in processors. It can be concluded that if the grids per processor are too low, it takes more time to transmit data by MPI communication.

7 Results and Discussion

8 Test Cases

Table 2 shows the icing condition cases selected for simulation using the OpenFOAM package and THERMSOLVICE code. Due to temperature conditions, Cases 27 and 33 lead to rime ice formation, while all others lead to glaze ice formation. The experimental and numerical data are available from NASA, DRA and ONERA for these cases [18].

Table 2: Icing condition cases on NACA0012 airfoil [18]

Case No.	Chord (m)	AOA (deg)	v_∞ (m/s)	T_∞ (K)	P_∞ (KPa)	LWC (g/m^3)	MVD (microns)	Exposure Time(s)
27	0.53	4.0	58.1	245.2	95.61	1.3	20	480
33	0.53	4.0	93.89	242.5	92.06	1.05	20	372
29	0.53	4.0	58.1	259.1	95.61	1.3	20	480
30	0.53	4.0	58.1	266.3	95.61	1.3	20	480
31	0.53	4.0	58.1	269.1	95.61	1.3	20	480
34	0.53	4.0	93.89	256.4	92.06	1.05	20	372
35	0.53	4.0	93.89	260.8	92.06	1.05	20	372

9 Convective Heat Transfer Coefficient

For the glaze ice cases, the convective heat transfer coefficients have to be estimated. To do so, the velocity gradients along the airfoil surface are obtained from the flowfield solution. Wall shear stress is calculated for the entire airfoil surface. The skin friction coefficient is computed as a function of shear stress, free stream velocity and air density. Because the flow is at four degrees angle of attack, the stagnation point is located on the airfoil lower surface downstream of the leading edge. The velocity has a zero value at the stagnation point, accelerating along the upper and lower airfoil surfaces. The velocity gradients have a minimum value at the stagnation point and increase along the upper and lower airfoil surface. Values of convective heat transfer coefficient are calculated based on the Reynolds analogy equation 4. The obtained values of heat transfer coefficient for glaze ice cases 29, 30, 31, 34 and 35 are in the same ranges and similar trends when compared with the literature [19, 20, 21, 22]. Figure 7 shows the values of convective heat transfer coefficient for the case 29 with two layers.

10 Collection Efficiency

Post-processing of droplet trajectory simulation provides the impingement limits, impingement region, number of impacting droplets, and their coordinates. The impingement limits identify the limiting trajectories where droplets inside these boundaries impinge the airfoil surfaces and those outside them do not hit the airfoil surfaces and move away from them. The impingement region is the surface area located between the impingement limits. The local collection efficiency (β) is the ratio of the distance between two droplets

at the release point to the corresponding distance between the same droplets along the airfoil surface. Equation 12 is used to calculate the values of collection efficiency along the impingement region. The total collection efficiency (β_{Total}) is defined as the ratio of the total distance between the limiting trajectories at the release point to the vertical distance between the impingement limits on the airfoil surface [23].

10.1 Case 27 with Four Layers

Figure 8 displays the prediction of collection efficiency using OpenFOAM for the rime ice case 27 with four layers. The collection efficiency curves are smooth in the first layer and have fluctuations for the second, third, and fourth layers due to ice formation. The smoothing technique by averaging method is used to minimize these fluctuations and obtain fitted collection efficiency curves. All collection efficiency curves have the maximum intensity of points close to the stagnation point and extend more along the lower airfoil surface.

10.2 Case 29 with Two Layers

Two-layer calculations of glaze ice cases are closer to experimental results than others for moderate exposure time. Figure 9 displays the collection efficiency values along the airfoil surface using OpenFOAM for the glaze ice case 29 with two layers. The collection efficiency curves are smooth for the first layer and has fluctuations in the second layer due to irregular shape of the ice surface. The maximum intensity of points close to the stagnation point. The number of water droplets in the first curve shows that the distribution of sticking droplets for the first layer is small along the upper surface, but large along the lower surface. The second curve shows that the distribution of water droplets for the second layer changes and the intensity of sticking droplets become high around the airfoil leading edge point on both upper and lower airfoil surfaces.

11 Thermodynamic Model Results

The transient ice thickness variations for glaze ice are obtained by numerical integrating of equation 38 using the numerical analysis code THERMSOLVICE. The results of case 29 with one-layer calculations are presented here to explain how the glaze ice properties change with time. The set of lines represents the history of icing on the airfoil segments within the impacting limits as shown in Figure 10. Segments are formed on the airfoil surface to identify the distances between the impinging droplets. In this case, 40 droplets impinge upon the airfoil surface; hence, 39 segments are formed. Segment 1 is the first panel at the upper impinging limit point and Segment 39 is the last panel at the lower impinging limit. The straight lines indicate rime ice type is found at the initial exposure time and for the segments which are far downstream from the stagnation point. In turn, the curved lines show glaze ice formation starting after a thin layer of rime ice at the stagnation point. This rime ice layer becomes thick behind the stagnation point along the upper and the lower surfaces. It can be observed that Segment 39 is purely rime ice, while Segment 15 changes from rime to glaze ice earlier than all other segments.

12 Comparison of Rime Ice Thickness Predictions with the Literature

The obtained results of rime ice predictions are computed based on droplet collection efficiency, free stream velocity and the exposure time [24]. The thickness of rime ice layers is ordered by the number of layers according to the exposure time. Figure 11a shows a comparison of the obtained rime ice results using OpenFOAM with the corresponding experimental and numerical data for the case 27. Comparison of rime ice results obtained using OpenFOAM with the corresponding experimental and numerical data for the case 33 are shown in Figure 11b. OpenFOAM simulation for both cases includes simulation with one, two, four and six layers. It can be seen that the predictions of ice shape and thickness are improved with dividing exposure time to multi layers. For single layer, the prediction of ice shape, impingement limits, ice volume and thickness are over-estimated. For two layers, there is an improvement in the prediction of ice shape and thickness at both sides, but has an over-estimation at the airfoil leading edge. For four and six layers, there is an improvement and matching in the prediction of ice shape and thickness in the most points of the experimental curve with slight over-estimation at the airfoil leading edge.

13 Comparison of Glaze Ice Thickness Predictions with the Literature

Glaze ice thickness for cases 29, 30, 31, 34 and 35 are computed using OpenFOAM and THERMSOLVICE code, and compared with the corresponding experimental and numerical data [18]. The thickness of glaze ice layers depends on the duration of exposure to the icing conditions and other icing factors. Figure 12 shows a comparison between the glaze ice results obtained using OpenFOAM modules and THERMSOLVICE code with the experimental and numerical data for all cases with two layers.The obtained results are reasonable and acceptable for all glaze ice cases with two layers. We can observe a good prediction of impingement limits, a good matching with the lower and upper parts of the experimental curve and at the leading edge, and slight under-estimation of the horns in cases 31 and 35. Although using multi-layer solutions should theoretically be more accurate than a single-layer solution, our experience with glaze ice formations showed that solutions after two layers gave less accurate results. This is attributed to the inaccuracies accumulated due to ice formation complexity at higher levels, which deteriorate mesh resolutions. In a similar fashion DRA has also reported that the glaze ice predictions with one layer gave better agreements with the experimental data than the multi-layer approach for the same test cases [18].

14 Effects of Iced Airfoil on Aerodynamic Coefficients

In-flight ice accretion on wings affects aerodynamic characteristics and aircraft performance. Rime ice and glaze ice which are formed on airfoil NACA0012 change the shape of the airfoil and affect significantly the lift and drag coefficients at high angles of attack. Reduction of lift force coefficient of iced airfoils and an increase in drag force coefficient compared with clean airfoils at different angles of attack are observed under the effect of

extreme changes in the airfoil shape and flow separation. Computed icing and experimental icing airfoils have low stall angles of attack and low maximum lift coefficient values than the clean airfoil values. In conclusion, airfoils with icing shape computed using OpenFoam give a similar effect with slight difference on aerodynamic coefficients when compared to the experimental ice shape effect. Figures 13 and 14 show the comparison of aerodynamic coefficients obtained using simpleFoam solver for clean and iced airfoils of rime ice cases 27 and 33.
Figures 15, 16, 17, 18 and 19 show the comparison of aerodynamic coefficients obtained using simpleFoam solver for clean and iced airfoils of glaze ice cases 29, 30, 31, 34, and 35.

15 Conclusion

In this study, we simulate ice accretion on aircraft wing surfaces using open-source packages in four modules: fluidflow module, trajectory module, thermodynamic and ice calculation module, and geometry updating module. An aerodynamic solver simpleFoam is used to simulate and solve the fluidflow within the boundary conditions of all icing cases. The Lagrangian solver icoUncoupledKinematicParcelFoam is used to simulate the trajectory of supercooled water droplets based on Newton's second law under the effect of gravity, buoyancy and drag forces. The coupling process between the fluidflow solver simpleFoam and the trajectory solver icoUncoupledKinematicParcelFoam solver is achieved. The heat transfer coefficient as a function of the skin friction coefficient and free stream velocity is calculated based on the Reynolds analogy for laminar and turbulent boundary layers. THERMSOLVICE code is developed to solve the governing equations of thermodynamic model. The main effects of ice accretion on the aerodynamic characteristics are investigated using simpleFoam simulation of iced airfoil with a wide range of angles of attack for all simulated cases. It was observed that large change in aerodynamic coefficients occur at high angles of attack due to significant flow separation. The main icing effects are increasing drag coefficient, reduction in maximum lift coefficient, altering pressure and velocity distribution around the airfoil, and reduction in stall angle of attack. These effects are resulted in degradation of aircraft performance and loosing of aircraft stability and controllability. The obtained results of convective heat transfer coefficient, collection efficiency and ice accretion shape and thickness for all simulated cases are in reasonably good agreement with the available literature, demonstrating that the open-source packages integrated here have the capability to predict the shapes and thicknesses of rime and glaze ice accretion problems with reasonable accuracy.

REFERENCES

[1] J. S. Alzaili, "Semi-empirical approach to characterize thin water film behaviour in relation to droplet splashing in modelling aircraft icing," 2012.

[2] E. Beld, "Droplet impingement and film layer modeling as a basis for aircraft icing simulations in openfoam," 2013.

[3] R. Hayashi and M. Yamamoto, "Two-and three-dimensional validation of icing model," 2013.

[4] G. Gori, M. Zocca, and A. Guardone, "A model for in-flight ice accretion based on the exact solution of the unsteady stefan problem," in *7th AIAA Atmospheric and Space Environments Conference*, 2015, p. 3019.

[5] H. Jasak, "Openfoam: open source cfd in research and industry," *International Journal of Naval Architecture and Ocean Engineering*, vol. 1, no. 2, pp. 89–94, 2009.

[6] C. J. Greenshields, "Openfoam user guide," *OpenFOAM Foundation Ltd, version*, vol. 3, no. 1, 2015.

[7] T. G. Myers, "Extension to the messinger model for aircraft icing," *AIAA journal*, vol. 39, no. 2, pp. 211–218, 2001.

[8] J. W. Eaton, D. Bateman, S. Hauberg, and R. Wehbring, *GNU Octave 4.0 Reference Manual*. Samurai Media Limited, 2015.

[9] S. Childress, *An introduction to theoretical fluid mechanics*. American Mathematical Soc., 2009, vol. 19.

[10] Z. Spakovszky, "16. unified: Thermodynamics and propulsion," *Unified Engineering*, 2009.

[11] C. R. Maliska, A. F. C. Silva, R. A. Silveira, C. N. Donatti, and G. Bridi, "Ice accretion prediction on aerodynamic bodies," in *IACC–International Aerospace CFD Conference, Paris*, 2007, pp. 18–19.

[12] J. Kim, P. G. Dennis, L. Sankar, and R. Kreeger, "Ice accretion modeling using an eulerian approach for droplet impingement," in *51st AIAA Aerospace Sciences Meeting including the New Horizons Forum and Aerospace Exposition*, 2013, p. 246.

[13] M. Kinzel, R. Noack, C. Sarofeen, and R. Kreeger, "A finite-volume approach to modeling ice accretion," in *28th AIAA Applied Aerodynamics Conference*, 2010, p. 4230.

[14] R. A. da Silveira, C. R. Maliska, and D. A. Estivam, "Aircraft icing simulation using navier-stokes and potential flow solutions for the external aerodynamics," 2004.

[15] R. A. Da Silveira, C. R. Maliska, D. A. Estivam, and R. Mendes, "Evaluation of collection efficiency methods for icing analysis," in *Proceedings of 17th International Congress of Mechanical Engineering*, 2003.

[16] R. Gent, N. Dart, and J. Cansdale, "Aircraft icing," *Philosophical Transactions of the Royal Society of London A: Mathematical, Physical and Engineering Sciences*, vol. 358, no. 1776, pp. 2873–2911, 2000.

[17] S. Ozgen and M. Canibek, "In-flight ice formation simulation on finite wings and air intakes," *The Aeronautical Journal*, vol. 116, no. 1178, pp. 337–362, 2012.

[18] W. B. Wright, R. Gent, and D. Guffond, "DRA/NASA/ONERA collaboration on icing research. part 2; prediction of airfoil ice accretion," 1997.

[19] Y. Bourgault, H. Beaugendre, and W. Habashi, "Development of a shallow-water icing model in fensap-ice," *Journal of Aircraft*, vol. 37, no. 4, pp. 640–646, 2000.

[20] Z.-H. Zhou, X. Yi, Y.-W. Gui *et al.*, "Study on the heat transfer characteristics in aircraft icing," *Procedia Engineering*, vol. 99, pp. 671–676, 2015.

[21] B. M. Berkowitz and J. T. Riley, "Analytical ice shape predictions for flight in natural icing conditions," 1988.

[22] D. Thompson and B. Soni, "Iceg2d: a software package for ice accretion prediction," in *41st Aerospace Sciences Meeting and Exhibit*, 2003, p. 1070.

[23] R. A. Da Silveira and C. R. Maliska, "Numerical simulation of ice accretion on the leading edge of aerodynamic profiles," in *Proceeding of the 2nd International Conference on Computational Heat and Mass Transfer COPPE/UFRJ, Brazil*, 2001.

[24] S. Edeeb, H. Akay, and S. Ozgen, "Rime ice shape predictions using openfoam," in *9th Ankara International Aerospace Conference*, 2017, p. 199.

[25] H. Adeli, "Introduction to parallel programming: Steven brawer," *Computer-Aided Civil and Infrastructure Engineering*, vol. 5, no. 4, pp. 327–327, 1990.

[26] C. Direct, "Openfoam user guide.[verkkodokumentti] viitattu 14.11. 2016," *Saatavissa: http://cfd. direct/openfoam/user-guide*, 2016.

[27] D. D. Knight, "Parallel computing in computational fluid dynamics," in *AGARD CONFERENCE PROCEEDINGS AGARD CP*. AGARD, 1996, pp. 3–3.

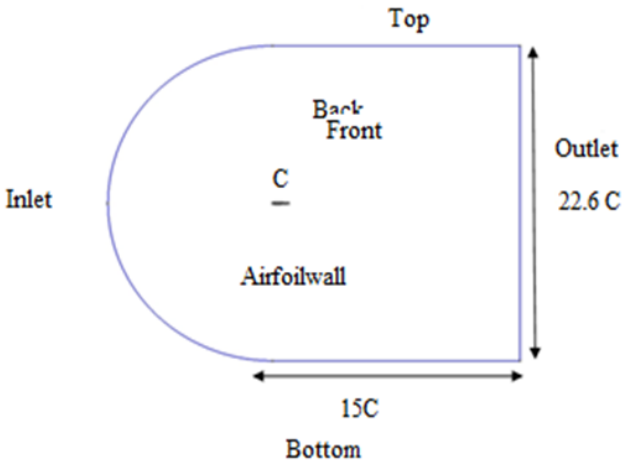

(a) Computational domain

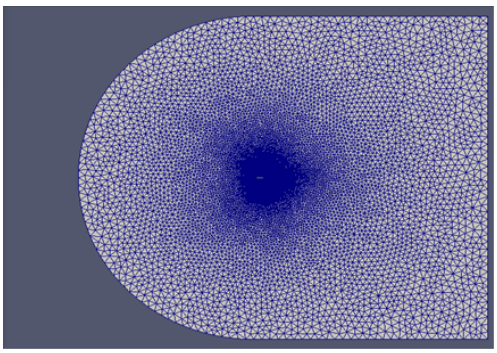

(b) Computational domain grids

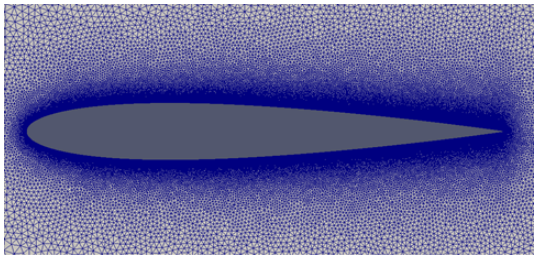

(c) Computational grids near the airfoil surface

Figure 1: Computational domain dimensions and mesh generation.

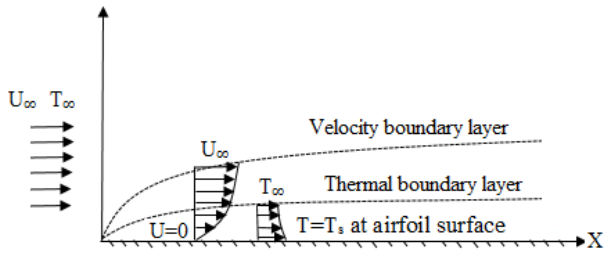

Figure 2: Velocity and temperature distributions close to the airfoil surface

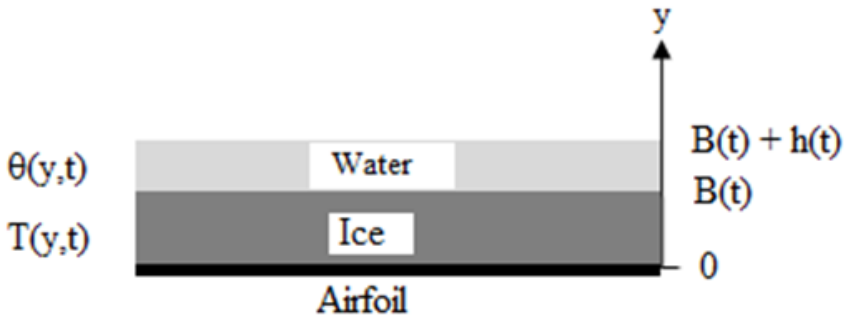

Figure 3: Ice and water layers

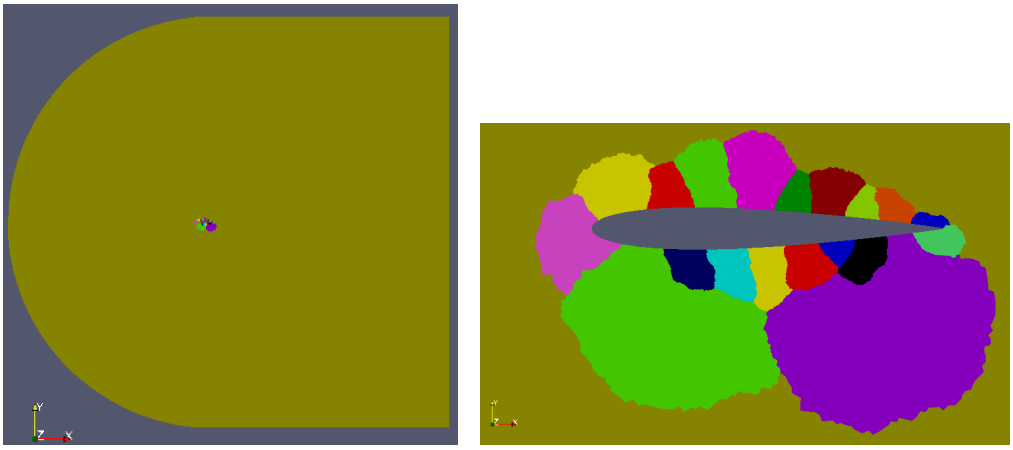

(a) Computational sub-domains (b) Sub-domains near the airfoil

Figure 4: Decomposition process using scotch method.

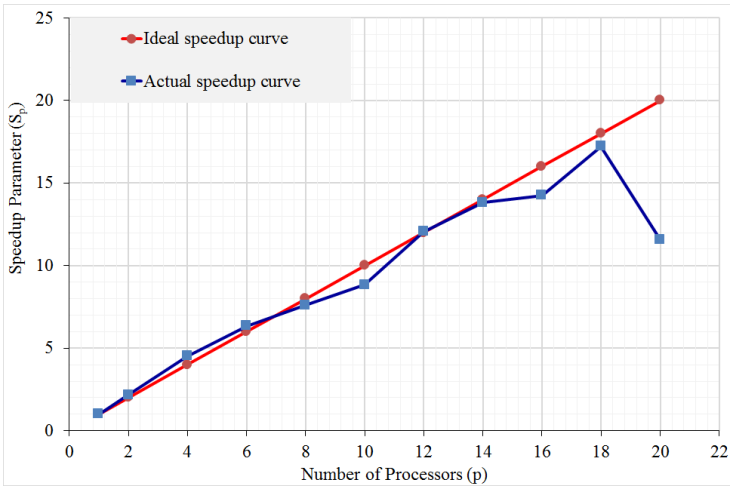

Figure 5: Speedup parameter values versus number of processors.

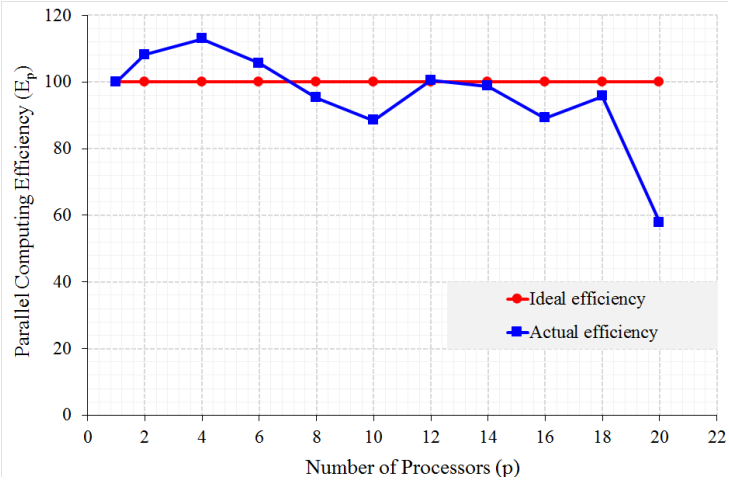

Figure 6: Performance efficiency parameter values versus number of processors.

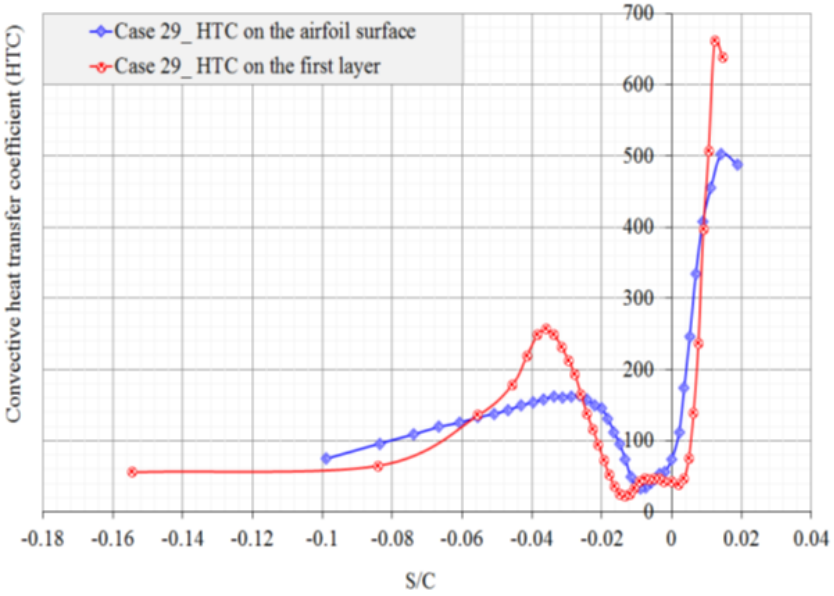

Figure 7: Convective heat transfer coefficient for the glaze ice case 29 with two layers

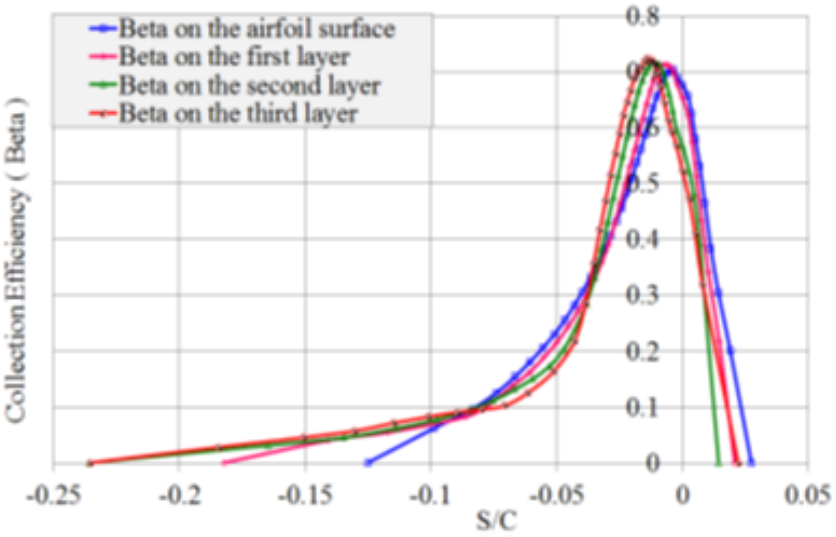

Figure 8: Collection efficiency for the rime ice case 27 with four layers

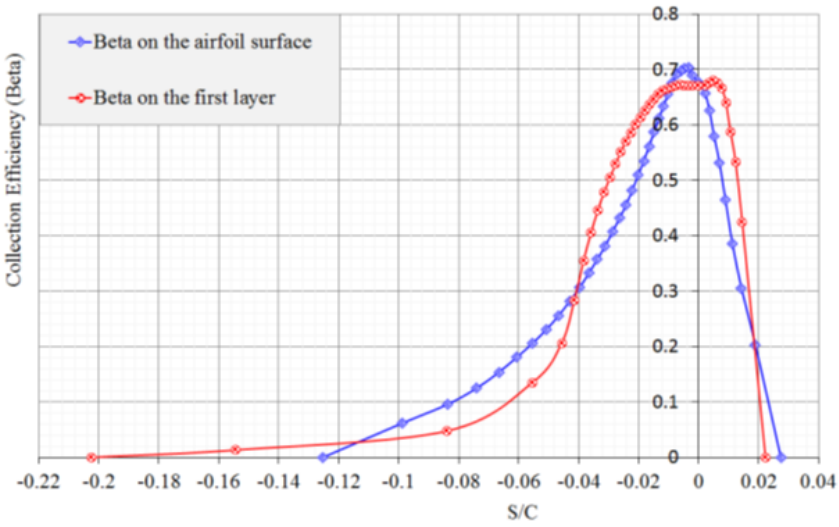

Figure 9: Collection efficiency for the glaze ice case 29 with two layers

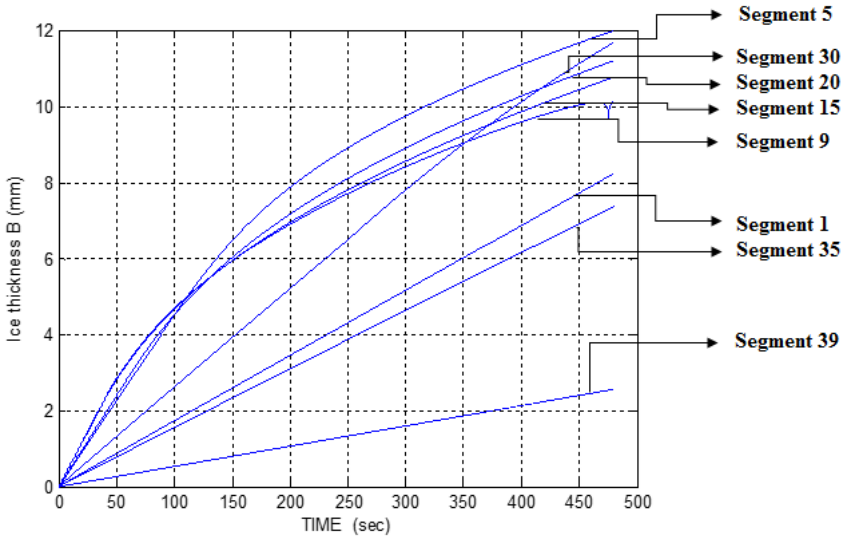

Figure 10: THERMSOLVICE code computation of ice thickness for the case 29 on the airfoil surface

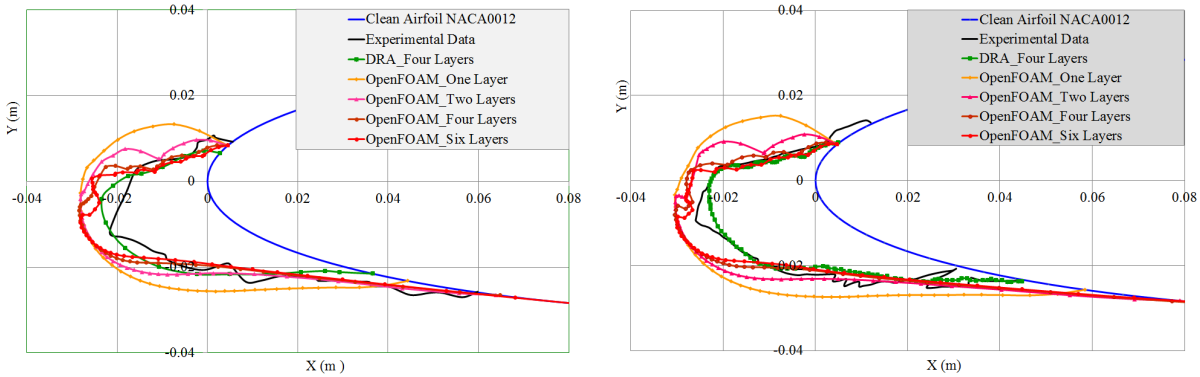

(a) Case 27 (b) Case 33

Figure 11: Comparison of rime ice thickness between OpenFOAM and literature

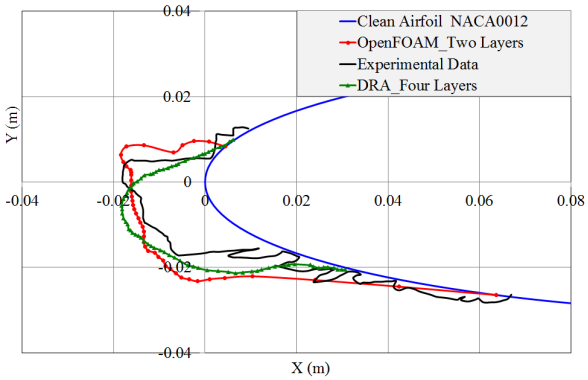

(a) Case 29

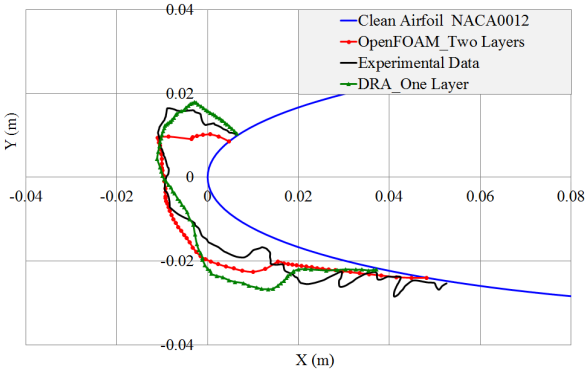

(b) Case 30

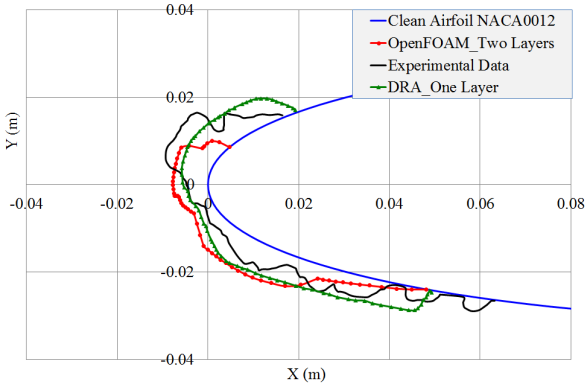

(c) Case 31

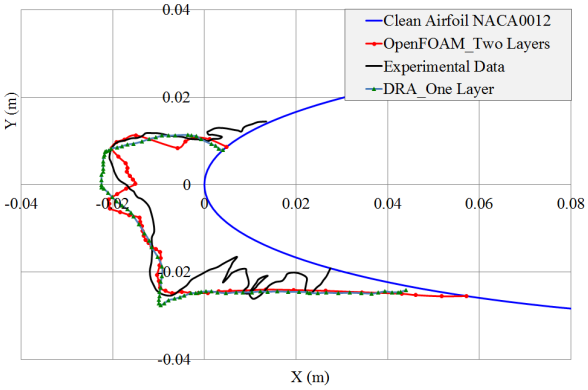

(d) Case 34

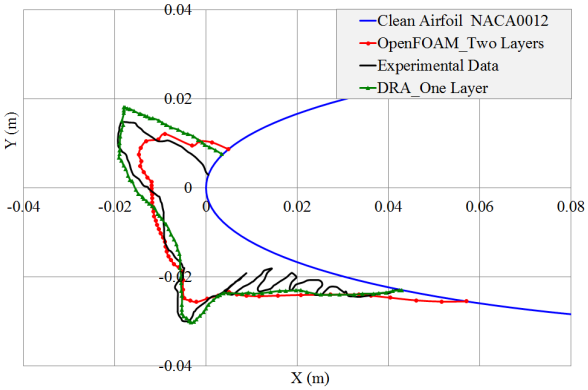

(e) Case 35

Figure 12: Comparison of glaze ice thickness between OpenFOAM with two layers and literature

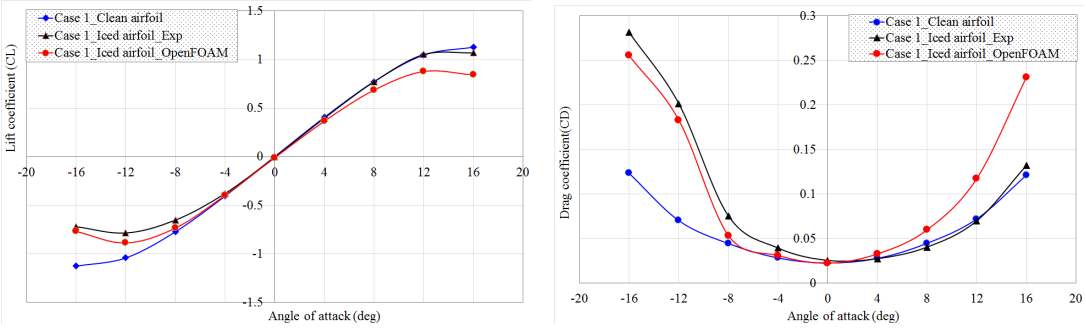

(a) Lift coefficient (b) Drag coefficient

Figure 13: Effect of rime ice shape on lift and drag coefficients for Case 27

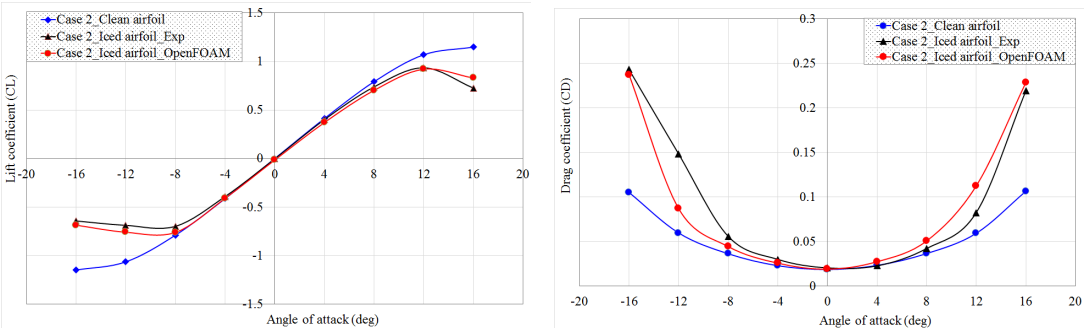

(a) Lift coefficient (b) Drag coefficient

Figure 14: Effect of rime ice shape on lift and drag coefficients for Case 33

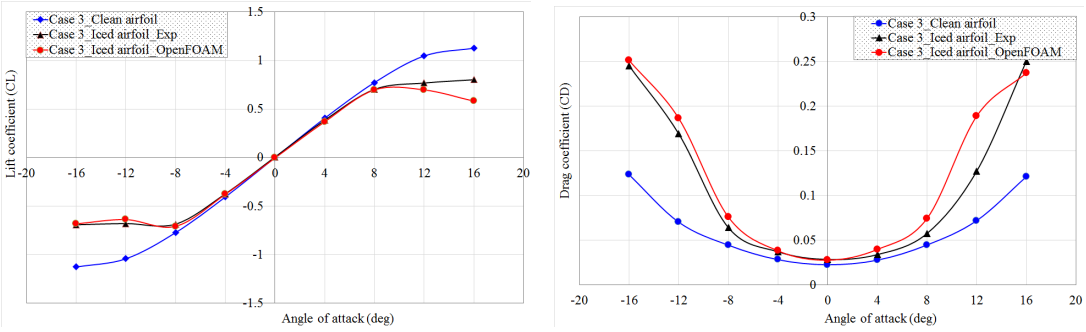

(a) Lift coefficient (b) Drag coefficient

Figure 15: Effect of glaze ice shape on lift and drag coefficients for Case 29

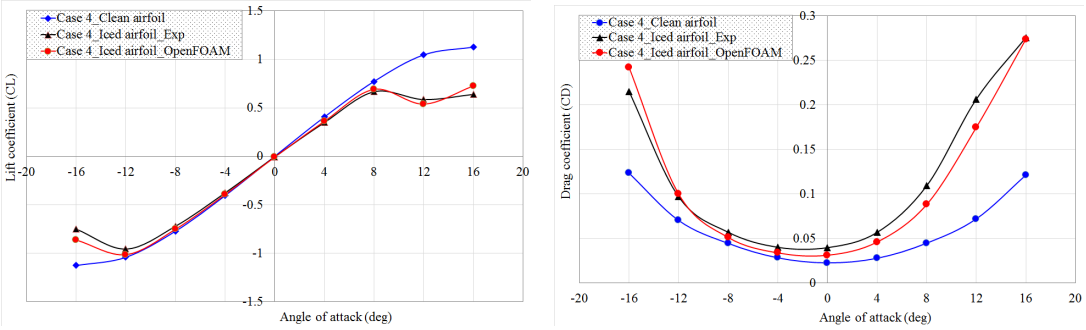

(a) Lift coefficient (b) Drag coefficient

Figure 16: Effect of glaze ice shape on lift and drag coefficients for Case 30

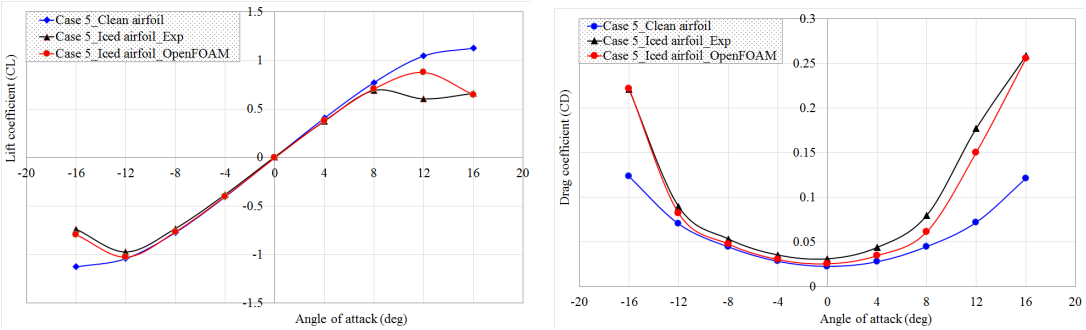

(a) Lift coefficient (b) Drag coefficient

Figure 17: Effect of glaze ice shape on lift and drag coefficients for Case 31

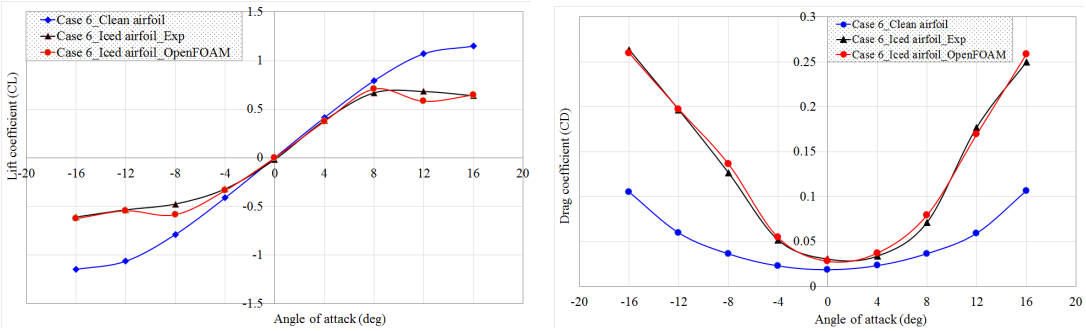

(a) Lift coefficient (b) Drag coefficient

Figure 18: Effect of glaze ice shape on lift and drag coefficients for Case 34

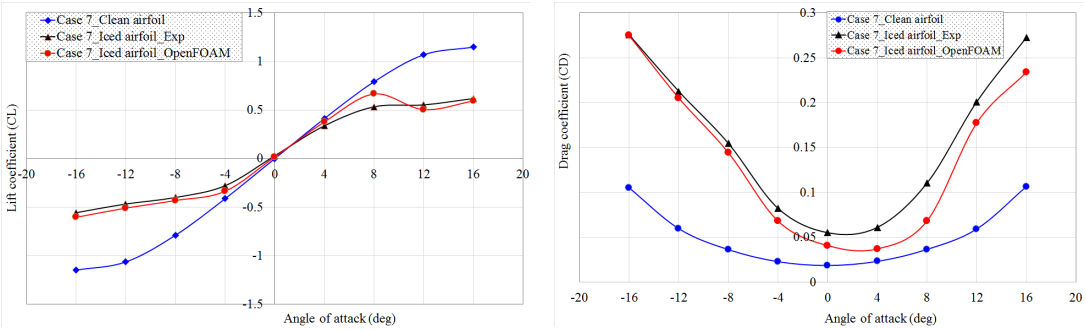

(a) Lift coefficient (b) Drag coefficient

Figure 19: Effect of glaze ice shape on lift and drag coefficients for Case 35